Seminar Indirect

Bouke Jung, Iris de Ruiter, Paul Hofland

June 2018

Contents

1 General introduction

It is commonly believed that most of the universe is made out of non-baryonic cold dark matter, which consist of Weakly Interacting Massive Particles (WIMPS). The most popular WIMP candidate still remains the neutralino, as predicted by the supersymmetric extension of the standard model (SUSY). These particles are often predicted in the GeV-TeV energy range and could be measured with two distinct methods; Direct and Indirect (note that no dark matter signal has been detected so far, but certain candidates have been either constrained or excluded [1]). The Direct measurement method looks for interactions between WIMPS and ordinary baryonic particles (such as Ge, NaI, Xe, CaF_2 molecules [2]), whereas the Indirect method looks for either gamma-rays, positions, antiprotons or neutrinos as signature. These particles are produced indirectly by pairs of WIMPs annihilations at dark matter halo locations in the galaxy. Although direct $\gamma\gamma$ or $Z\gamma$ annihilation lines are in theory possible, they are loop-suppressed. Therefore, most of the gamma-rays will follow the annihilation of pairs of quarks, leptons or Higgs bosons. The methods are complementary to each other. However, uncertain astrophysical background sources can create issues for the latter method. In this review we will discuss various methods to indirectly detect dark matter. We will describe the theoretical framework for each of these methods, the observational results and make predictions for the future.

2 Gamma-ray experiments

One of the ways to indirectly detect dark matter particles is to look for the gamma-ray signature of their annihilation. Two dark matter particles can annihilate to two standard model particles which then decay and leave a distinct signature in gamma-rays. Using gamma-ray telescopes that point to different regions of the sky with different optimal energy ranges, we can probe the dark matter content within the local universe. Gamma-rays are extremely powerful in creating a dark matter density map of the Universe since they are not deflected by magnetic fields, contrary to e.g. cosmic rays.

In section 2.1 we will discuss how the expected gamma-ray flux depends on the dark matter cross section and mass. Comparing the corresponding formulae to observations, it is possible to set an upper limit to the dark matter mass and cross section by the absence of an annihilation signal. In section 2.2 different complications in translating observation data to actual dark matter densities are discussed. Furthermore some typical examples of dark matter density profiles are explained. Finally in section 2.3 the current and future gamma-ray telescopes, and their efforts on constraining the dark matter parameters, are discussed.

2.1 Gamma-ray flux from dark matter WIMP annihilation - (Paul Hofland)

As said before, we will consider neutral WIMPs that only interact trough gravitational force and annihilate into Standard Model particles via the weak interaction. Gamma rays are one of the decay products of this annihilation. The energy and angle dependent gamma-ray brightness for this annihilation process is given by formula 1:

$$I_\gamma(E,\Theta)\& = \frac{1}{2}\frac{\langle\sigma v\rangle}{m_{DM}^2}\frac{dN_{\gamma,ann}}{dE_\gamma}\frac{1}{4\pi}\int dl\rho_{DM}^2(r[l,\Theta]) \tag{1}$$

where the first half of equation 1 depends on the particle physics model of dark matter (i.e. particle physics) and the second half on the dark matter distribution (i.e. astrophysics).

2.1.1 Particle physics factor

The velocity-averaged dark matter pair annihilation cross section $\langle\sigma v\rangle$ can be estimated by looking at the relic abundance observed today due to freeze-out and linking this to the pair annihilation rate

of dark matter, which implies $\langle \sigma v \rangle \sim 3 \times 10^{-26} cm^3 s^{-1}$, see formula 4 [3].

$$\Omega_{DM} h^2 \sim \frac{3 \times 10^{-27} cm^3 s^{-1}}{\langle \sigma v \rangle} \qquad (2)$$

The differential spectrum of emitted gamma-rays per annihilation, $\frac{dN_{\gamma,ann}}{dE_\gamma}$, can be seen as the sum (weighted by branching ratio, see formula 3) of all spectra final states, see figure 1. Since the branching ratio and final states are very model dependent, there are major uncertainties involved in trying to explain all observable dark matter using a single WIMP dark matter candidate. The differential spectrum is given by

shouldnt it be -26 in this eqn?

$$\frac{dN_{\gamma,ann}}{dE_\gamma} = \sum_i B_i \frac{dN^i_{\gamma,ann}}{dE_\gamma} \qquad (3)$$

where B_i is the model depended branching ratio, and $\frac{dN^i_{\gamma,ann}}{dE_\gamma}$ the individual final state spectra.
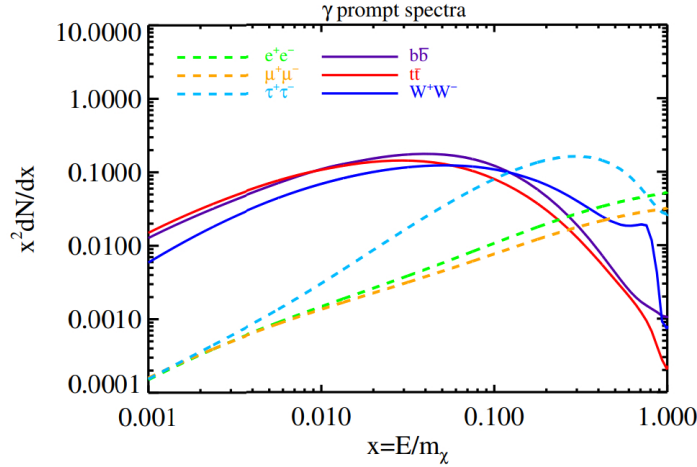

Figure 1: Figure from [3]: Gamma-ray spectrum from dark matter ($m_{DM} = 500 GeV$) annihilation to six different final states, calculated using PPPC4DMID [4]

The gamma-ray brightness also contains a factor $\frac{1}{2}$, which implies that dark matter is its own anti-particle, this would be a factor $\frac{1}{4}$ otherwise. And lastly dividing by m^2_{DM} cancels out the density squared integral from the astrophysical factor.

2.1.2 Astrophysical factor

The second half of the gamma-ray brightness (formula 1), consist only of the so called J-factor, which describes the amount and distribution of dark matter in a particular source. More exact; it is the line of sight integral over the dark matter density squared (ρ^2_{DM}) at an angle from the line of sight, see formula 4 for its definition.

$$J = \frac{1}{\Delta\Omega} \int \int_{\Delta\Omega} \rho^2_{DM}(l, \Omega) dl d\Omega \qquad (4)$$

Note that in formula 1, the factor $\frac{1}{4\pi}$ is a normalization factor that comes from integrating over solid angle.

The dark matter density functions (ρ_{DM}) are dependent on the physical situations and only depend on the radial distance to the center of the dark matter source, r. This will be explained in greater

detail in chapter 2.3. To compute the line of sight integral, we first need to relate R to L and Θ (see figure 2).
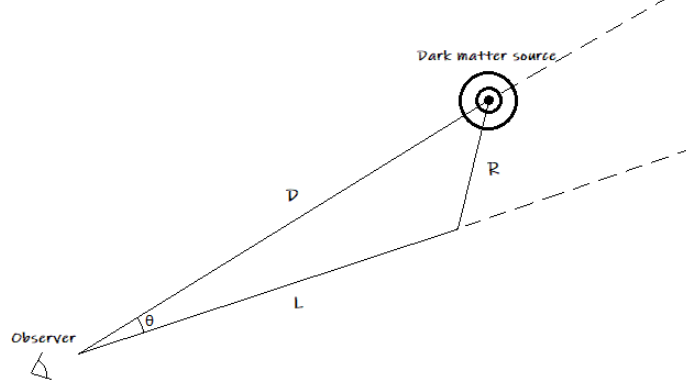

Figure 2: Top down view of observer looking down the line of sight with some angular separation Θ at a dark matter source.

Using D to denote the distance to the dark matter source and writing L for the line of sight, R for shortest distance from the line of sight to the center of the source and Θ for the angular separation of the source, we can relate R to L and Θ using the cosine rule to get formula 5.

$$R = \sqrt{L^2 + D^2 - 2L\cos\Theta} \tag{5}$$

Looking back at the total gamma-ray brightness (formula 1) and comparing this to the annihilation rate per volume, see formula 6. It becomes clear that formula 1 is just the annihilation rate per volume times the total differential spectrum of emitted gamma-rays integrated over some volume.

$$\text{Rate of annihilation per volume: } \frac{1}{2}\frac{\langle\sigma v\rangle\rho_{DM}^2}{m_{DM}^2} \tag{6}$$

2.1.3 Sagittarius gamma-ray flux

To conclude this section we show an example of a computed gamma-ray flux spectrum as a function of dark matter mass (m_χ) per annihilation channel for dwarf galaxy Sagittarius [5] (see figure 3).
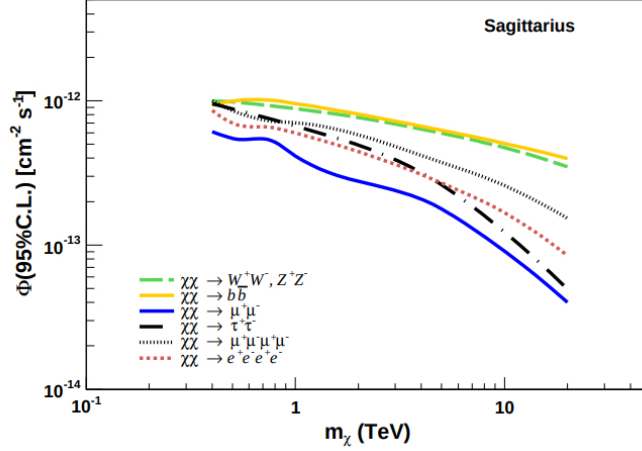
Figure 3: Figure from [5]: Gamma-ray flux as a function of dark matter mass (m_χ) for different annihilation channels.

Note that the gamma-ray flux scales with $1/m_{DM}^2$, and therefore scales down exponentially with mass. In other words; higher WIMP mass means less annihilation processes per dark matter source and therefore less gamma-rays.

2.2 Probing Dark Matter Distributions - Bouke Jung

Having discussed the theoretical background of indirect dark matter signals, the natural question arises how these signals actually manifest in the observable universe. A proper answer can only be provided in the context of the distribution of dark matter within the local universe. After all, one expects to observe a brighter gamma-ray signal in regions with high dark matter density.
Over the past decades great effort has been made to model and constrain the distribution of dark matter within the Milky Way and surrounding astrophysical objects. A few examples of recent findings are given by the discovery that the Milky Way does not conform to density profiles created from adiabatic compression [6] and the fact that neighbouring dwarf galaxies seem to exhibit dark matter distributions which become constant towards their galactic center [7]. Perhaps even more groundbreaking was the work of Diemand et al. (2008), who found evidence for the fact that dark matter can cluster together locally, forming complicated substructures which boost gamma-ray production by over an order of magnitude and cosmic ray production by a typical factor of 1.4 [8].

In this section we'll summarize some of the most prevalent models used in the context of indirect dark matter studies. Before explaining the various parameters and equations involved, however, we will first take another look at the relation between observed gamma-ray spectra and underlying dark matter distributions, in an attempt to form a better understanding of the difficulties involved with inferring flux rates from certain dark matter density profiles and vice versa.

2.2.1 Translating observational data to DM densities

The gamma-ray fluxes detected at observatories such as Fermi-LAT and the future CTA in principle contain all the information one needs in order to map dark matter distributions across galactic planes and large scale structures. As we've seen in section 2.1, there exists a direct theoretical correspondence between a source's gamma-ray intensity and the line-of-sight integral over the dark matter density. However, this is not the whole story. In making a direct comparison between the line-of-sight integral and observational fluxes, we implicitly neglect several processes of radiative transfer which could have

lead to redistribution of initial dark matter generated gamma-ray fluxes — not to mention the fact that some gamma-ray detections could be misinterpreted as indirect dark matter signals, having a completely different origin all the while! Hence, in order to derive accurate conclusions regarding dark matter distributions via gamma-ray fluxes, we first have to discuss radiative transfer effects. Additionally we have to exclude the possibility of misinterpreting background signals.

Once a gamma-ray has been created through dark matter annihilation or decay, several processes might occur to it which alter the gamma-ray's energy before it reaches an observatory. Most prominent are perhaps compton scattering and pair production. In the latter case, particle-antiparticle pairs (usually electrons and positrons) are formed out of two photons. A quick order-of-magnitude calculation reveals that if the dark-matter-induced gamma-ray would undergo such a process together with a typical 2.7 Kelvin photon of the comsic microwave background (CMB) (i.e. $k_B \cdot T \approx 8.6 \cdot 2.7 \approx 10^{-4} eV$) whilst traveling through the interstellar medium, it would need to have an energy of at least $E_{\gamma,1} \cdot E_{\gamma,2} \approx E_{\gamma,1} \cdot 6.6 \cdot 10^{-4} eV \approx m_e^2 \approx 2.5 \cdot 10^{11} eV^2$. Hence, the photon initially created from dark matter annihilation or decay, would be required to have an energy greater than a few hundred TeV. For space-based gamma-ray observatories such as Fermi-LAT, which generally operate at energies of a few hundred MeV to several hundred GeV, this process should therefore not constitute any impairment in detecting dark-matter-induced gamma-rays. The upcoming Cherenkov Telescope Array (CTA) which is planned to operate between a few hundred GeV and a few hundred TeV, might have to take the process into account.
Compton scattering may form a problem when the produced gamma-rays travel through areas in interstellar space with high electron densities. Typically, however, induced effects will not be very dramatic. Taking a characteristic electron density of a few particles per cubic centimetre and assuming that the Thomson approximation holds[1] we see that the optical depth associated with Compton scattering for a source at a distance of a few kpc would be:

$$\tau \approx n_e \sigma_T h d \approx 1 \, \text{cm}^{-3} \cdot 1 \times 10^{-24} \, \text{cm}^2 \cdot 1 \times 10^{22} \, \text{cm} \approx 10^{-5}$$

Hence we can conclude that galaxies are typically very optically thin when it comes to compton scattering. This allows one to largely ignore such processes in studying indirect dark matter signals, provided that the gamma-rays one observes did not have to propagate through any dense interstellar regions.

2.2.2 Dark matter distribution profiles

Provided that any ambiguities in ones signal have been thoroughly discussed and ruled out, it is in principle possible to construct dark matter density profiles for astrophysical objects using formula 2.1. Usually, however, researchers take the density profile as an input parameter and try to reproduce observed emission spectra numerically for comparison purposes. Over the years, a variety of different models have come into use [3]. The most recognizable one is perhaps the *Navarro-Frenk-White* (NFW) profile:

$$\rho_{NFW} = \frac{\rho_0}{\left(\frac{r}{r_s}\right)\left[1 + \left(\frac{r}{r_s}\right)\right]^2} \tag{7}$$

where r denotes the distance from the center of the galactic halo and r_s is a scale radius, indicatiing the point where the logarithmic derivative of the radial density profile becomes equal to -2. In the case of the Milky Way, Fornasa and Green (2014) [9] established that $r_s \approx 20 \, \text{kpc}$, resulting in a dark matter density at the sun's position of around $0.4 \, \text{GeV/cm}^3$ and Pato et al. (2015)

---

[1]To be precise one would need to input the Klein-Nishina cross section for this scattering process. However, since the Thomson cross section is always bigger, we can use $\sigma_T h$ instead to retrieve an upper limit.

Some slightly more involved profiles try to account for various deviations that cannot be modeled accurately by a pure NFW denisty profile. Particularly they create steeper profiles at the inner edges of the dark matter halo, since mechanisms involving (gravitational) interactions between dark matter and baryonic matter such as adiabatic contraction are expected to yield more concentrated dark matter distributions towards the galactic center [10, 11, 12]. Generalizing equation 2.2.2 and allowing for an arbitrary inner slope γ, we get the formula:

$$\rho_{GNFW} = \frac{\rho_0}{\left(\frac{r}{r_s}\right)^\gamma \left[1 + \left(\frac{r}{r_s}\right)\right]^{3-\gamma}} \tag{8}$$

which reverts back to equation 2.2.2 for $\gamma = 1$. Observationally, we typically find that $0 \leq \gamma \leq 1.5$, where $\gamma = 0$ corresponds to a so-called *coned* profile, whilst $\gamma = 1.5$ is also refered to as a Moore profile [13, 14].

Contrary to the above two profiles, more recent simulations seem to suggest that galactic dark matter density profiles deviate from simple power-law dependencies, displaying slopes that vary with radius instead [15, 16, 17]. One of the first attempts at modeling such irregularity was made by *Einasto* [18], who used the formula:

$$\rho_{Ein}(r) = \rho_0 \exp -\frac{2}{a} \left[\left(\frac{r}{r_s}\right)^a - 1\right] \tag{9}$$

Observations for the Milky Way yield values around 0.2 for the parameter α.

One last dark matter density profile that we'll have to discuss is provided by *the Burkert profile*:

$$\rho_{Burk}(r) = \frac{\rho_0}{\left(1 + \frac{r}{r_s}\right)\left(1 + \left(\frac{r}{r_s}\right)^2\right)} \tag{10}$$

This model distinguishes itself from the rest, because it quickly flattens towards the galactic core. Since many dwarf-galaxies display density profiles which strongly deviate from power-law distributions, the Burkert formula is used very frequently in the context of these objects. Considering that spheroidal dwarf galaxies generally consist of a very low density, homogeneously distributed gas, it should come as no surprise that their (dark) matter density becomes nearly constant towards the center.

Figure 4 displays the various dark matter density profiles discussed within this section in a single panel. The differences between each of the profiles is clearly visible. The GNFW profile is the steepest and leads to large densities at the galactic core. Meanwhile, the Burkert density profile quickly flattens as the radius decreases, conform our expectations for an elliptic dwarf galaxy, which generally constitute relatively low mass, and homogeneous companion galaxies to a main host.

2.3 Current and future gamma-ray telescopes and their constraints on the dark matter cross-section - (Iris de Ruiter)

As said before we hope to detect dark matter particles via their annihilation signature. Two dark matter particles can annihilate to two standard model particles which then decay and leave a distinct signature in gamma-rays. Gamma-ray telescopes focus on the detection of gamma-rays from this dark matter annihilation process. This process is usually split up into multiple channels. The most important examples are $\chi\chi \to b\bar{b}$ and $\chi\chi \to \tau^+\tau^-$. The constraints given on the mass and cross section for the dark matter particle are given for each of these annihilation channels (bottom quarks and tau leptons), where the tau channel usually gives the strongest constraints. In the search for
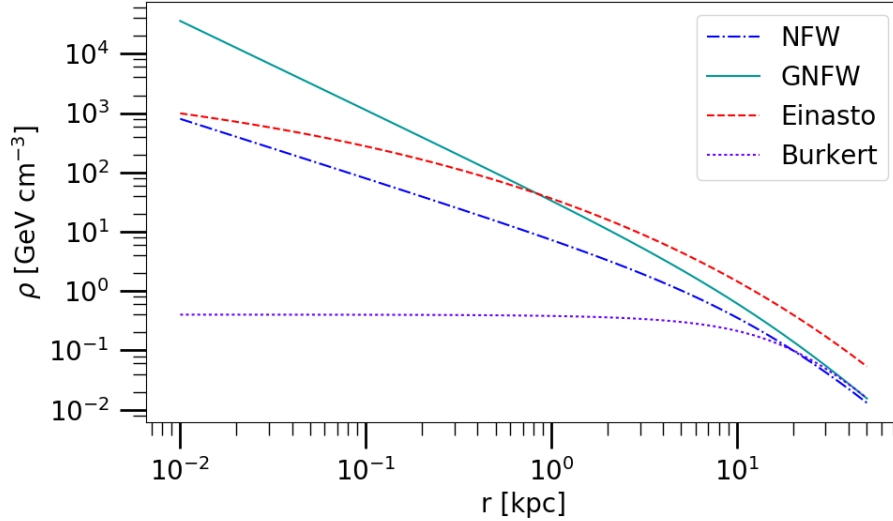
Figure 4: A graph of the various dark matter density profiles discussed within section 2.2.2. All profiles are generated using an input density $\rho_0 = 0.4$ and a scale radius $r_s = 20\,\text{kpc}$. Additionally, the GNFW spectrum was given an index $\gamma = 1.5$, whilst the Einasto spectrum received an index $a = 0.2$.

these annihilation processes most observations look directly at the dark matter halo of our Milky Way since this is one of the most dark matter dense regions (see section 2.2.1). Another way to get observations of dark matter dense regions is to observe regions around intermediate-mass black holes with masses in the range $10^2 \leq M/M_\odot \leq 10^6$, since there are enhancements (mini-spikes) of the dark matter densities around these black holes [19]. In the sections below we will discuss specific gamma-ray telescopes and their efforts in dark matter research.

2.3.1 Fermi-LAT

Most of our knowledge of gamma-ray emission from dark matter annihilation comes from the Fermi-LAT telescope. The LAT, which stands for Large Area Telescope, is the primary instrument on the Fermi Gamma-ray Space Telescope mission. It has a wide field-of-view for high-energy gamma-rays and it covers the range from below 20 MeV to more than 300 GeV [20]. The Fermi-LAT telescope is able to directly detect the gamma-ray emission via pair production. Observation of the Milky Way halo with Fermi-LAT provided some of the strongest constraints on the mass and cross section of the dark matter particles in the past [21].

Nowadays the best results come from the observation of dwarf spheroidal satellite galaxies (dSphs) of the Milky Way, which are some of the most dark matter dominated objects known. The lack of detection of gamma-rays gives us an upper limit to the dark matter cross section. Section 2.1 explains how the flux is related to the cross section. The newest Fermi-LAT data provide some of the most robust constraints on the dark matter mass.

For the $b\bar{b}$ annihilation channel they find $m_{DM} \gtrsim 1$ TeV and the dark matter cross section $\langle \sigma v \rangle \lesssim 1 \cdot 10^{-26} cm^3 s^{-1}$, for the $\tau\tau$ channel they find $m_{DM} \gtrsim 70$ GeV and the dark matter cross section $\langle \sigma v \rangle \lesssim 4 \cdot 10^{-26} cm^3 s^{-1}$ [22]. The results are summarized in figure 5, where the confidence intervals in the mass - cross section plane are shown for the two annihilation channels. The constraints from this publication take into account the uncertainty in the dark matter distribution of the dSphs. The Fermi-LAT telescope will be able to further constrain the mass and cross section by observing the dSphs in longer observation runs and the discovery of new dSphs.
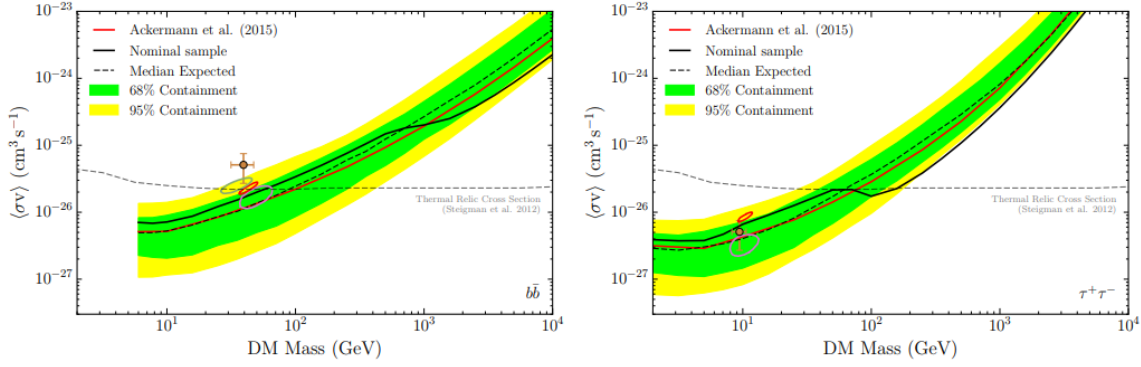
9

Figure 5: Figure from [22]: Constraints on the DM annihilation cross section at 95% CL for the $\chi\chi \to b\bar{b}$ (left) and $\chi\chi \to \tau^+\tau^-$ (right) channels derived from a combined analysis of 15 dSphs. Bands for the expected sensitivity are calculated by repeating the same analysis on 300 randomly selected sets of high-Galactic-latitude blank fields in the LAT data. The dashed line shows the median expected sensitivity while the bands represent the 68% and 95% quantiles. The solid black line shows the observed limit from the combined analysis of 15 dSphs from [23].The dashed gray curve in this figure corresponds to the thermal relic cross section from [24].

2.3.2 H.E.S.S.

Another important gamma-ray telescope is the H.E.S.S., which is an acronym for the High Energy Stereoscopic system. As opposed to the Fermi-LAT this is a ground based Imaging Atmospheric Cherenkov Telescope, which allows for much larger telescopes but also causes interference of the atmosphere with the gamma-ray detections. The H.E.S.S. collaboration shows a great evolution for constraints on the dark matter parameters over time. One of the first papers from 2006 concluded that there was no significant gamma-ray excess in the galactic center of the Milky Way [25]. In a 2011 publication they exclude cross sections larger than $\langle\sigma v\rangle = 3 \cdot 10^{-25} cm^3 s^{-1}$ for a dark matter mass of $m_{DM} \sim 1$ TeV [26]. The latest H.E.S.S. publication gives the strongest constraint on the dark matter cross section in for a $m_{DM} \sim 1$ TeV so far. The upper limit is given to be $\langle\sigma v\rangle = 4 \cdot 10^{-28} cm^3 s^{-1}$ [27].

2.3.3 VERITAS, MAGIC and HAWC

Other gamma-ray telescopes are also able to place constraints on the dark matter cross section, but these are usually less constrictive then the Fermi-LAT and the H.E.S.S. limits. VERITAS and MAGIC are both Imaging Atmospheric Cherenkov Telescope similar to H.E.S.S. but smaller in size. The HAWC is the High Altitude Water Cherenkov telescope, which uses water tanks to detect Cherenkov light from incoming gamma-rays as opposed to the atmosphere like H.E.S.S., VERITAS and MAGIC. The advantage of this technique is the ability to continuously run measurements at a wider field of view, instead of only at night (darkness is needed of atmospheric Cherenkov imaging).

The latest VERITAS papers constrain the cross section for the bottom quark channel to $\langle\sigma v\rangle = 1.35 \cdot 10^{-23} cm^3 s^{-1}$ and for the tau lepton channel to $\langle\sigma v\rangle = 1.32 \cdot 10^{-25} cm^3 s^{-1}$ at $m_{DM} \sim 1$ TeV [28]. As said before the recent constraints from the H.E.S.S. collaboration are about 10^{-3} times more rigid. The MAGIC collaboration finds a strongest constraint in the tau lepton annihilation channel as well: $\langle\sigma v\rangle = 3.8 \cdot 10^{-24} cm^3 s^{-1}$ at $m_{DM} \sim 0.5$ TeV [29]. Finally there is HAWC which only started observing recently and therefore has not produced constraints nearly as strong as other telescopes yet [30].

2.3.4 Future telescopes

In the near future the Cherenkov Telescope Array (CTA) hopes to improve the current limits set by H.E.S.S [32]. The CTA experiment will be the largest Imaging Atmospheric Cherenkov Telescope, taking into account telescope arrays in the northern and southern hemisphere. Since these telescopes vary in size, the CTA will improve sensitivity over a large energy range. They will be able to constraint the dark matter cross sections for dark matter masses ranging from 100 GeV to tens of TeV, with a sensitivity improved by a factor of 5-10 [32]. Fig. 6 shows how the CTA will hope to improve the dark matter cross section over a wide energy range. The sensitivity is shown in comparison with the strongest Fermi-LAT and H.E.S.S. constraints. It is important to note that these predictions are made by the CTA consortium itself. Critics of these optimistic constraints say that the actual CTA cross section constraints will be an order of magnitude weaker than estimated by the CTA consortium [33]. Here the galactic diffuse gamma-ray emission and systematic errors that will decrease the CTA sensitivity are properly taken into account.
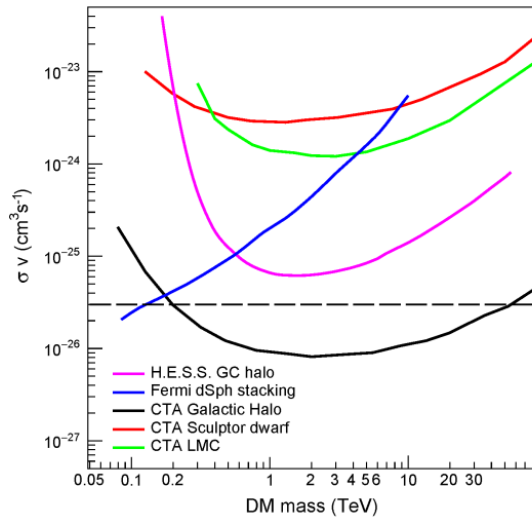

Figure 6: Figure from [31]: comparison of predicted sensitivities in for the targets of: the Milky Way Galactic halo: the Large Magellanic Cloud (LMC) and the dwarf galaxy Sculptor. The CTA sensitivity curves use the same method and W^+W^- annihilation modes for each target and the Einasto dark matter profile. The sensitivities for the three targets are all for 500 hours taking into account the statistical errors only.

Other planned gamma-ray telescope arrays include the CALET, GAMMA-400 and HERD. The first two telescopes have been launched recently and will improve the current resolution in small energy ranges [34, 35]. They will however not be able to improve the limits on the continuous spectrum, as set by Fermi-LAT. The HERD telescope is set to launch in 2020, and will be the most sensitive gamma-ray telescope in the 10 GeV to 1 TeV range [36]. At higher energies the Cherenkov telescopes will do better, since they have a larger effective area.

2.3.5 Comparison of gamma-ray telescopes

Table 1 shows a comparison of the discussed current (top) and future (bottom) gamma-ray telescopes in energy range, field of view, constraints on dark matter masses and cross sections.

Table 1: Comparison of different current (top) and future (bottom) gamma-ray telescopes in energy range, field of view (f.o.v.), constraints on dark matter masses and cross sections. The right column shows the references for these parameters. *: $\frac{2}{3}$ of the sky. **: these are the optimistic constraints as set by the CTA consortium. Critics thinks that the actual cross section constraints will be up to an order of magnitude higher [33]. ***:geometric factor $> 3m^2$ sr.

Name	Energy range	F.o.v ($°$)	m_{DM}	σv (cm^3/s)	Ref
Fermi-LAT	20 MeV - 300 GeV	4.2	~ 10 GeV	$\sim 4 \cdot 10^{-26}$	[20], [22]
H.E.S.S	300 GeV - 70 TeV	3.5	~ 1 TeV	$4 \cdot 10^{-28}$	[27]
Veritas	85 GeV - 30 TeV	3.5	~ 1 TeV	$2.85 \cdot 10^{-24}$	[28]
Magic	100 GeV - 100 TeV	3.5	~ 0.5 TeV	$3.8 \cdot 10^{-24}$	[29]
HAWC	500 GeV - 100 TeV	*	~ 1 TeV	$\sim 10^{-24}$	[30]
CTA	100 GeV - 10 TeV	4-5	~ 1 TeV	$5 \cdot 10^{-27} - 3 \cdot 10^{-26}$ **	[31], [32]
CALET	100 GeV - 1 TeV	45-58	—	—	[34]
GAMMA400	20 MeV - 1 TeV	60	—	—	[35]
HERD	10 GeV - 1 TeV	***	10 GeV 1 TeV	$6 \cdot 10^{-30} - 5 \cdot 10^{-29}$ $4 \cdot 10^{-27} - 9 \cdot 10^{-27}$	[36]

3 CMB constraints on dark matter

Another way to possibly detect dark matter is via its imprint on the Cosmic Microwave Background (CMB). Around the time of recombination ($z \sim 1000$) the secondary particles of dark matter annihilation would have affected other processes and therefore would have left an imprint on the CMB [37]. One of the biggest achievements of modern cosmology is the remarkable agreement between the theoretical description of recombination and the observations of the CMB. Our standard model of recombination is severely constrained by the CMB data, ie. changing the recombination model while staying in agreement with the CMB data has proven difficult [38]. Examples of refinements to the current recombination model are delayed recombination [39] and accelerated recombination [40], both of which turned out to correspond badly with the available CMB data. Measurements of the CMB by WMAP and more recently by Planck are able to put constraints on dark matter models.

3.1 Cosmological history with the CMB power spectrum

Figure 7 shows the theoretical CMB power spectrum, compared to the most recent Planck data [41]. As said before, one of the greatest achievements of modern cosmology is the remarkable agreement between our current ΛCDM model (red) and data (blue). We can even use this agreement to constrain the dark matter cross section. To do so it is important to fully understand the (bumps in the) CMB power spectrum and how they are affected by altering the theoretical input.
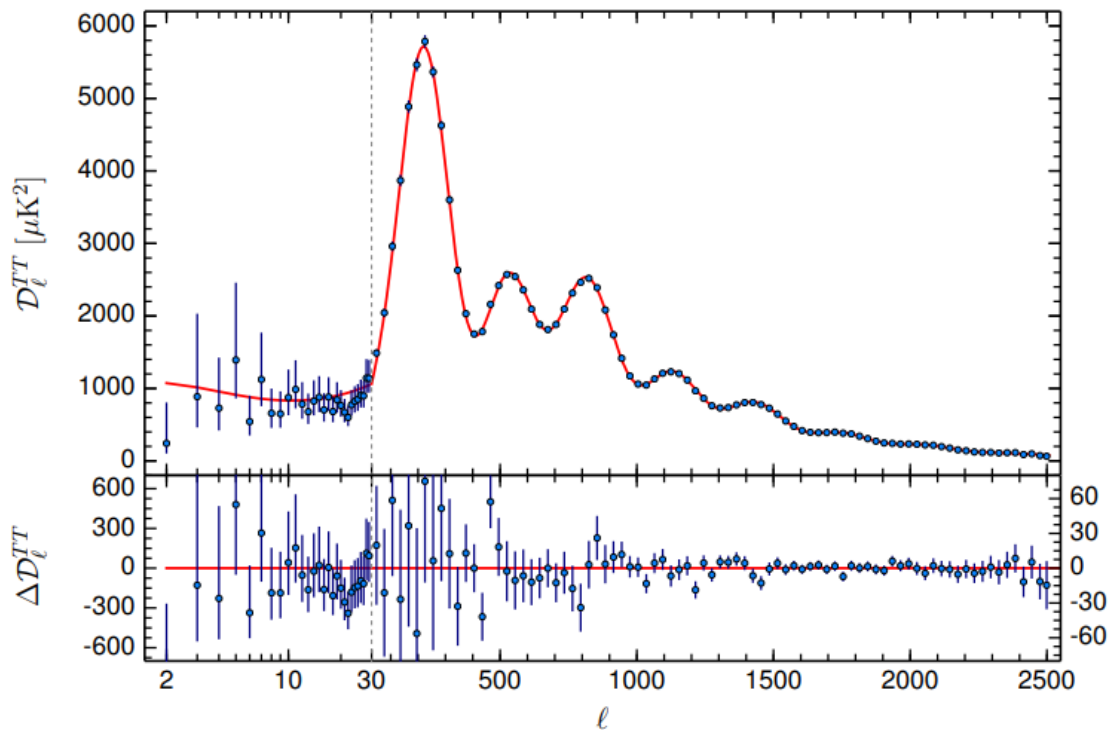

Figure 7: Planck 2015 CMB spectra, compared with the base ΛCDM fit to Planck data (red line). The upper panel show the spectra and the lower panel shows the residual. The horizontal scale changes from logarithmic to linear at the "hybridization" scale, $\ell = 29$. We show $\mathcal{D}_\ell = \ell(\ell+1)C_\ell/(2\pi)$ as a function of the angular scale ℓ. [41]

The Cosmic Microwave Background is a faint glow of the era of decoupling of the early universe (380000 years after the Big Bang). At this point in time the temperature of the Universe had dropped enough for electrons and protons to form hydrogen and the Universe became opaque to photons. This afterglow of recombination nowadays has an average temperature of 2.725 K, but small fluctuations are present. Figure 7 shows the angular power spectrum of these temperature fluctuations. It shows that the angular fluctuations with the largest amplitude lie around $\ell = 200$. At higher ℓ the amplitude peaks again at around $\ell = 700$ and $\ell = 850$, which implies that temperature fluctuation at this angular scale are louder than other angular scales. These peaks in the power spectrum give valuable information about the physics in the early Universe.

The first peak shows the imprint and oscillation pattern of sound waves in the baryon fluid in the early Universe. This fluid was affected by gravity and radiation pressure, which respectively pulled the fluid together or pushed it away. The pushing and pulling of radiation and gravity causes a profound oscillation pattern. The way this oscillation pattern is found in the CMB is affected by the curvature of the universe. In a closed universe the light from hot spots (large amounts of matter at the time of decoupling) will bend in such a way that they appear larger in the CMB, and vice versa. Comparing our expectations of the oscillation pattern at this scale and observations of the CMB we find that our universe is flat [41].

The second and third peak contain information about the amount of regular and dark matter in the universe. At these scales the oscillating pattern is being damped. This damping is due to diffusion of photons at the time of decoupling from matter. This decoupling process was not instantaneous but took a few tens of thousands of years. During this period, photons and other particles were still interacting, though not as frequently as before decoupling. This small interaction rate scattered the photons and therefore damped the imprint of the oscillation pattern at small scales. The amount of damping of the second and third peak compared to the first, gives insight in the amount of baryonic and dark matter in the Universe.

After decoupling from photons from matter, the Universe began its so-called Dark Age. This epoch is called Dark since there were only two radiation sources. One was the slowly redshifting CMB, the other were photons occasionally released by neutral hydrogen atoms. The latter mechanism is known as the 21 cm line of hydrogen. During the Dark Ages gravity was acting on matter to clump it in high density regions, that were able to form stars and galaxies. The Dark Ages slowly evolved into the next epoch, where actual stars and galaxies gradually formed. This lead to the event over reionization: the radiation of the first stars reionized the surrounding universe. Neutral hydrogen atoms were split into a plasma of electrons and protons again. During this reionization the Universe remained largely transparent, and this epoch ended slowly due to the expansion of the Universe.

3.2   Dark matter annihilation at recombination

The structure and equations of this section are based on [37] and [42]. The annihilation of dark matter particles affects the ionization history of the Universe in three different ways. The interaction of the decay shower from the annihilation products with the thermal gas can either ionize the gas, induce a Ly-α excitation of hydrogen or simply heat the plasma. Figure 8 schematically shows the possible outcomes of dark matter annihilation. In this discussion we neglect the neutrino contribution, since they do not interact with the inter galactic medium (IGM). Ionization and Ly-α excitation influence the evolution of the free electron fraction x_e, while the heating of the plasma only affects the baryon temperature. Adjusting the expression for the evolution of the ionization fraction x_e for annihilation particles we find:

$$\frac{dx_e}{dz} = \frac{1}{(1+z)H(z)} \left[R_s(z) - I_s(z) - I_\chi(z) \right] \tag{11}$$

14

where R_s is the standard recombination rate, I_s the ionization rate by standard sources, and I_χ is the new term that accounts for the ionization rate due to particle annihilation. The first two terms are standard expressions, available in most CMB codes. See for example [43] and [44] which are based on [45].

The interesting addition to this equation is the ionization rate due to in this case the annihilation of dark matter particles. This ionization rate happens both by direct ionization from the ground state ($I_{\chi_i}(z)$) and by adding additional Ly-α photons to the plasma ($I_{\chi_\alpha}(z)$). These photons will increase the rate of photo-ionization by the CMB from the exited states. Therefore I_χ can be split up into two parts $I_\chi(z) = I_{\chi_i}(z) + I_{\chi_\alpha}(z)$.

Figure 8: Figure from [46]: The injection of energy from dark matter annihilation into the IGM, via the creation of electromagnetic cascades. Energy transfer to the IGM takes place principally through the ionization and collisional processes.

The power output per unit volume by a self-annihilation dark matter particle is given by

$$\frac{dE(z)}{dVdt} = \rho_c^2 c^2 \Omega_{DM}^2 (1+z)^6 f \frac{<\sigma v>}{m_\chi} \qquad (12)$$

As before $<\sigma v>$ is the effective velocity averaged cross section of the dark matter particle with mass m_χ. Ω_{DM} is the dark matter density parameter, ρ_c is the critical density of Universe today and the f parameter indicates the energy fraction that is absorbed overall by the gas. From here it is possible to relate $I_{\chi i}(z)$ and $I_{\chi \alpha}(z)$ to the power output:

$$
\begin{aligned}
I_{\chi i} &= C\chi_i \frac{[dE/dt]}{n_H(z)E_i} \\
I_{\chi \alpha} &= (1-C)\chi_\alpha \frac{[dE/dt]}{n_H(z)E_\alpha}
\end{aligned}
\qquad (13)
$$

Here $\chi_i = \chi_\alpha = (1-x_e)/3$ are the fractions of energy going to ionizations and Ly-α photons respectively, $n_H(z)$ is the number density of hydrogen nuclei, E_i is the average ionization energy per baryon and E_α is the difference in binding energy between the 1s and 2p energy levels of a hydrogen atom. Incorporating formulae 12 and 13 in formula 11 yields a simple extension with the dark matter ionization rate to the standard evolution of the ionization fraction.

This extension of the ionization fraction is useful since we can compare it to current models and data and find how big certain dark matter parameters (such as $<\sigma v>$ and m_χ) can be before we find significant deviations. Therefore we can place upper limits on these parameters.

3.3 Sommerfeld enhancement

An example of the contribution of CMB analysis to our understanding of dark matter is the exclusion of Sommerfeld enhancement. In 2008 a positron excess was observed by the PAMELA satellite [47]. This excess was attributed to the signature of dark matter annihilation, where the dark matter cross-section had to be enlarged via the Sommerfeld enhancement [48, 49]. In more recent work by [50] it is shown that dark matter annihilation can not be the cause of the positron excess. They conclude this based on the limits from the μ-type distortion of the CMB energy as observed by the FIRAS (Far Infrared Absolute Spectrophotometer) instrument on the COBE (Cosmic Background Explorer) satellite.
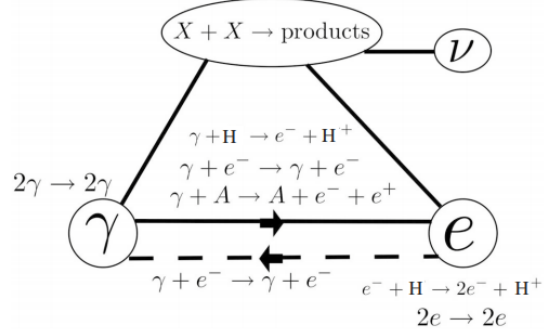
3.4 Cosmological signatures of DM self-annihilation - Bouke Jung

Having discussed the theoretical link between dark matter annihilation and the thermal history of the universe, we have all the tools we need to investigate potential footprints of the involved dark matter processes within acquired observational data. Of particular interest are the observations procured by the Planck satellite between 2009 and 2013. Having provided the highest sensitivity mappings of CMB anisotropies to date, this satellite has enabled researchers to put stringent upper limits on dark matter effective self-annihilation rates. Not surprisingly, in recent years we have seen the publication of several papers dedicated towards constraining DM annihilation parameters via Planck satellite data [51, 52]. This subsection is dedicated towards summarizing some of the most important findings.

3.4.1 Methodology

Before diving into the various results on dark matter self-annihiliation derived from cosmic microwave background data over the last years, let us first recapitulate on the methodology often applied in CMB indirect DM searches. In section 3.2 we saw that DM annihilation holds considerable sway over the course of cosmological history in the sense that the process may have injected vast amounts of energy into the intergalactic medium (IGM) at certain redshifts. From an observational point of view, this is important, since it might have lead to detectable defects in a diverse range of cosmological measurements, such as the baryonic matter and dark matter densities, the CMB angular power spectrum, the temperature of the intergalactic medium, as well as the optical depth towards the epoch of reionization. Of particular relevance to induced changes in all of these parameters, is the quantity:

$$p_{ann} \equiv f \frac{<\sigma v>}{m_\chi} \tag{14}$$

which was already encountered in equation 12. Since p_{ann} is directly coupled to the DM annihilation ionization rates by virtue of equation 11, the parameter will cause different evolution schemes of the free electron fraction x_e for different values. In the literature this is often modeled using the recombination coding routine *RECFAST* [53].
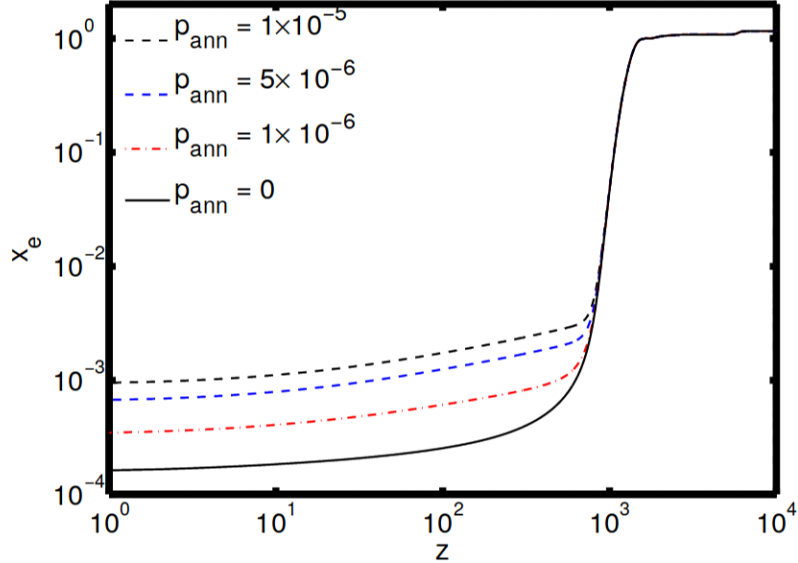

Figure 9: The evolution of the free electron fraction as a function of redshift for different values of $p_a nn$, as presented in Galli et al. (2009) [37].

Figure 9 displays the evolution of x_e for different values of p_{ann}. Evidently, values as small as $p_{ann} = 1 \times 10^{-5}$ can introduce up to an order of magnitude difference in the ionization fraction at redshifts $z < 10^3$ (before the epoch of recombination). This goes to show the impact that dark matter annihilation can have on cosmological history.

In close correspondence with the free electron fraction, the CMB angular power spectrum will also vary between different values of p_{ann}. This is perhaps best understood by looking at optical depth. If the number density of free electrons is indeed enhanced by dark matter self-annihilation, the optical depth towards the last scattering surface of the CMB photons will naturally increase. As a consequence we will have to deal with a larger opacity when measuring the CMB, causing the amplitude in the angular power spectrum to decrease.

Figure 10 displays how the temperature (TT) and E-mode polarization (EE) CMB angular power spectra as well as the temperature and E-mode polarization cross spectrum (TE) vary for different dark matter annihilation schemes. As we predicted earlier, the acoustic oscillations within the angular power spectra become damped whenever there is a non-trivial dark matter annihilation rate. More interesting to note is the fact that there exists little difference between the curves with equivalent values of $< \sigma v > /m_\chi$. This has to do with the fact that the f-parameter in equation 14 varies very little over the redshift range where scattering of CMB-photons is most likely (i.e. between around $z \sim 800$ and $z \sim 1200$[2]). As a consequence, the acoustic oscillations of the power spectra are only truly affected by the average value of f around $z \sim 1100$, which happens to be nearly equal for all dark matter WIMP candidates with equal annihilation-rate-to-mass ratio $< \sigma v > /m_\chi$.

In order to formulate a definitive answer to the question which model for dark matter annihilation holds the most merit (i.e. which value of p_{ann} yields the most sensible numbers for CMB observables), one has to confer with observational data in some way or another. Usually this is accomplished via a series of maximum likelihood fits to the parameters:

$$\{\Omega_{b,0}h^2, \Omega_{DM,0}h^2, \Theta_s, z_{reio}, n_s, \ln\left[10^{10}A_s\right], < \sigma v >, m_\chi\} \tag{15}$$

where $\omega_b \equiv \Omega_{b,0}h^2$ stands for the baryonic matter density, $\omega_{DM} \equiv \Omega_{DM,0}h^2$ denotes the dark matter density and Θ_s describes the ratio between the angular sound horizon and the angular diameter to decoupling[3]. Furthermore, z_{reio} stands for the redshift to the start of reionization, n_s indicates the scalar spectral index, $\ln\left[10^{10}A_s\right]$ indicates the logarithmic amplitude of the primordial power spectrum[4], $< \sigma v >$ denotes the thermally-averaged DM annihilation cross-section and m_χ describes the DM mass. A Markov Chain Monte Carlo (MCMC) analyzation method allows one to sample values for each of the cosmological parameters ω_b, ω_{DM}, Θ_s z_{reio}, n_s and A_s, such that WMAP and PLANCK CMB observational data are fitted best.

In figure 11 we see the constraints derived by Galli et al. for the baryonic and cold dark matter density as well as the scalar spectral index using the five-year WMAP satellite data in 2009. Although the cold dark matter density does not seem to be affected by the inclusion of dark matter annihilation, the baryonic matter density and the scalar spectral index are clearly subjected to a shift. For an upper limit $p_{ann} < 2.0 \times 10^{-6}\,\mathrm{m}^3/\mathrm{s}/\mathrm{kg}$ we see that the constraint on ω_b changes from $\omega_b = 0.0228 \pm 0.0006$ to $\omega_b = 0.0230 \pm 0.0006$, whilst the limits on n_s change from $n_s = 0.965 \pm 0.014$ to $n_s = 0.977 \pm 0.018$.

---

[2]This is explained in more detail Hütsi et al. (2011) [54]. In particular, see the sharp peak of the visibility function around $z \sim 1100$ in figure 2 of the same paper.

[3]With *the sound horizon* we refer to the characteristic length scale of the CMB accoustic oscillations, which are given by the comoving distance that a sound wave can travel between the Big Bang and recombination [56].

[4]The *scalar spectral index* n_s and the amplitude A_s usually come up when discussing primordial density fluctuations. In this context, the power in density fluctuations with wavenumber k is generally assumed to behave as $P(k) = A_s(k/k_\star)^{n_s-1}$, where $k_\star = 0.05\,\mathrm{Mpc}^{-1}$ denotes a reference scale and where $n_s = 1$ corresponds to a situation of *scale-invariant* fluctuations.
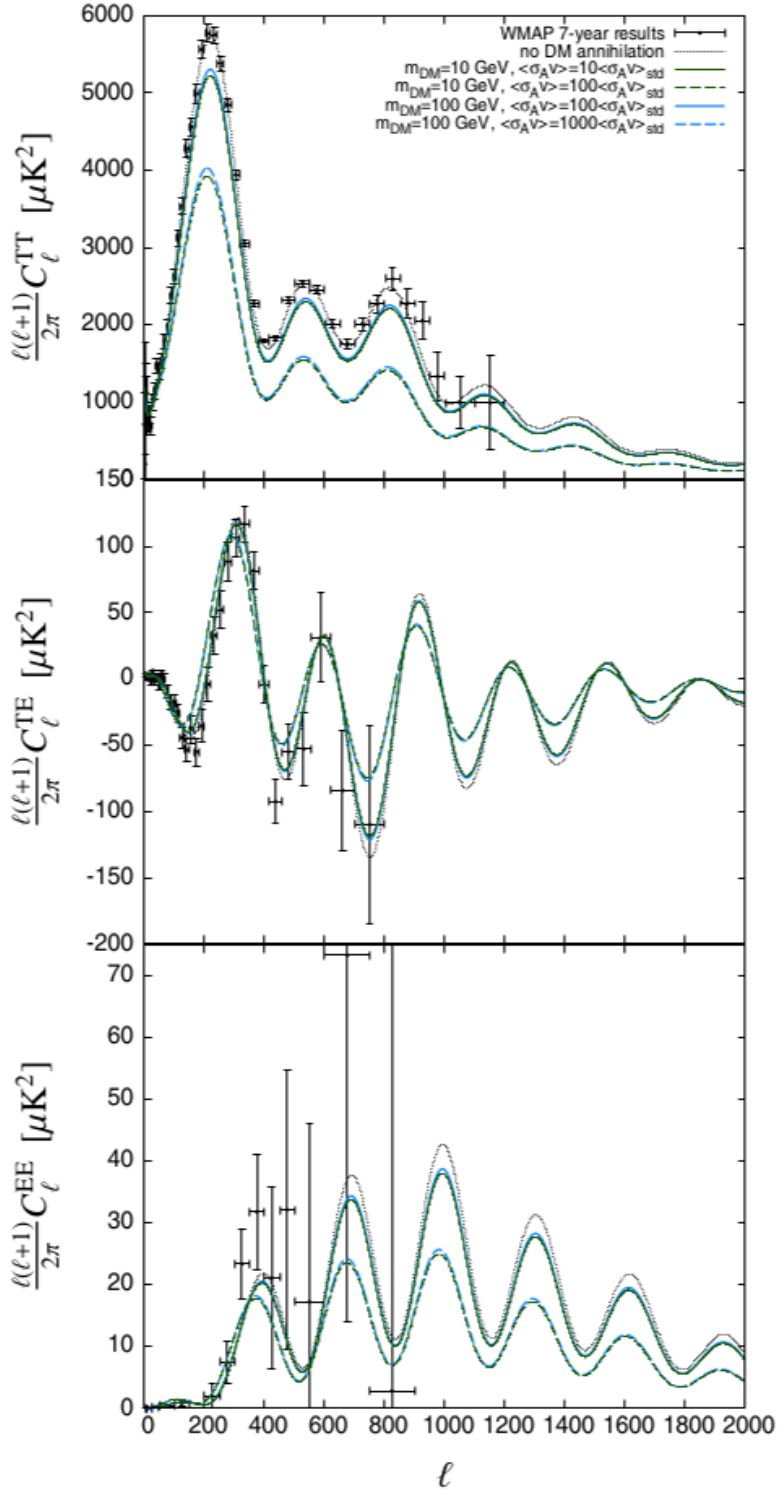
Figure 10: Angular power spectra of the CMB as presented in Hütsi et al. (2011) [54] for different dark matter masses and annihilation rates. From top to bottom we have (i) the angular power spectra derived for the CMB temperature anisotropies, (ii) the temperature and E-mode polarization cross-spectra and (iii) the E-mode polarization spectra. Dotted lines show theoretical predictions for the ΛCDM model [55], whilst the points with errorbars indicate 7-year measurements conducted by the WMAP space mission.

18

Figure 11: The 1-D likelihood distributions of the baryonic matter density, the scalar spectral index and the cold dark matter density as derived in Galli et al. (2009) [37] using the five-year WMAP dataset. Solid lines indicate results in the case of standard recombination, whilst dasheed lines show constraints including dark matter annihilation.

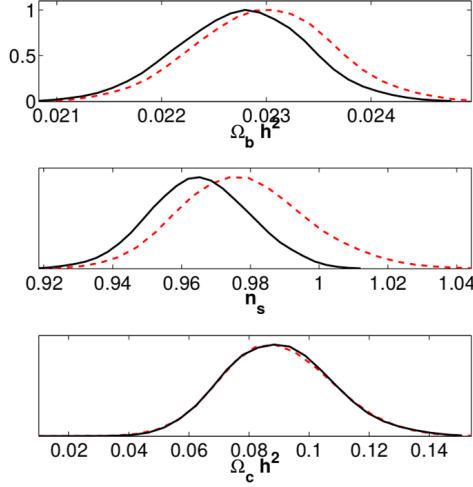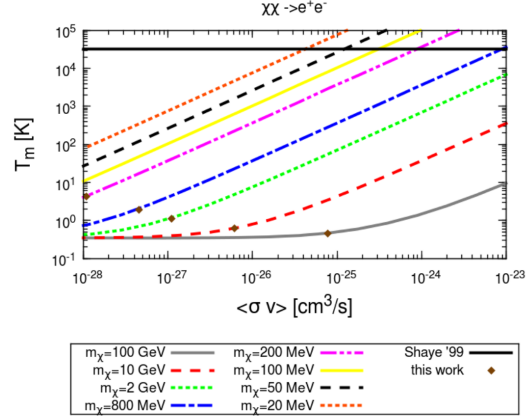Figure 12: Dark matter annihilation constraints on the IGM temperature T_m as presented in Lopez-Honorez (2013) [57], assuming annihilation occurs into e^+e^- pairs solely and $z_{reio} = 10$. Brown diamond indicate upper limits obtained for $< \sigma v >$ using WMAP9+SPT11+HST+BAO data, whilst a black solid line shows the $T_m = 32\,000\,\mathrm{K}$ upper limit derived from Ly-α observations at $2 < z < 4.5$.

These results conform to what one might expect qualitatively. After all, in the presence of DM annihilation into standard model particles, the overall baryonic matter content of the universe ought to increase. Furthermore, the net decrease in dark matter during the period of inflation, will result in generally greater density fluctuations, since the gravitational potential associated with regional matter overdensities will decrease. This yields a larger value of n_s, which is reflected by the graph in figure 11.

Some more recent papers, incorporating the latest data by WMAP and PLANCK give constraints on $\ln\left[10^{10}A_s\right]$ and the IGM temperature T_m, similar to the ones discussed above for n_s, ω_b and ω_c. Of particular interest are figures 12 and 13, which can be found in Lopez-Honorez (2013) [57] and in Madhavacheril et al. (2014) [52] respectively. As can be seen, lower DM particle masses and higher annihilation rates lead to higher IGM temperatures. This makes sense, considering that greater values of p_{ann} lead to increased energy injection rates, as we saw previously in equation 12. Another interesting fact to note is that the dark matter annihilation rate decreases, whenever the DM particle mass goes down (see the brown datapoints in the plot). This is of course caused the decrease in energy phase space, which makes the annihilation process less efficient.
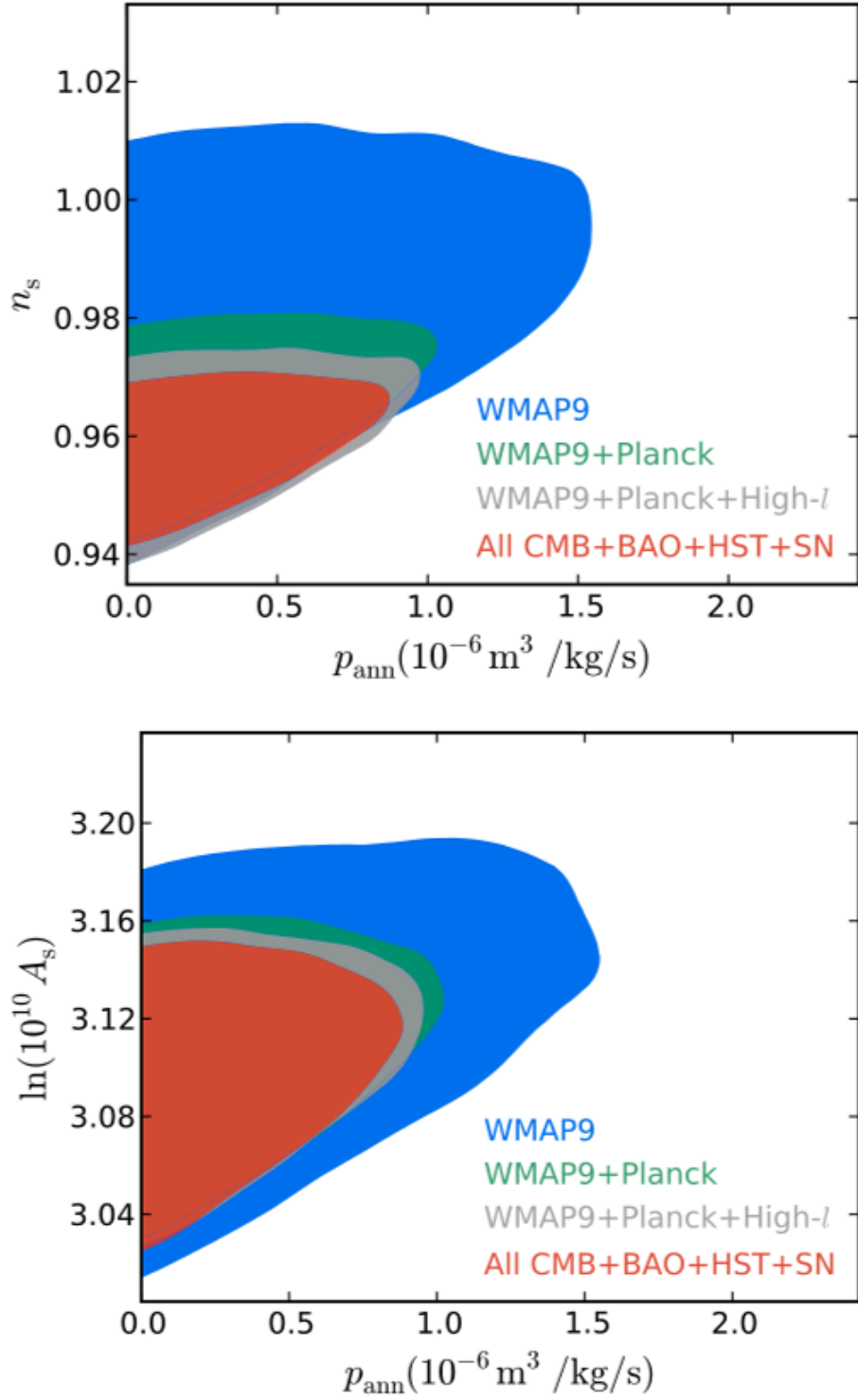
Figure 13: 95% confidence limit contours for n_s and $\ln\left[10^{10}A_s\right]$ as a function of p_{ann} as derived by Madhavacheril et al. in 2014 [52] for selected combinations of datasets.

3.5 Observational constraints of self-annihilation cross-section from WMAP and PLANCK data

From the constraints on p_{ann} that come from maximum likelihood parameter fitting (see chapter 3.4.1) and using equation 14, we find the following velocity averaged annihilation cross-section $< \sigma v >_r$ at recombination as a function of dark matter mass m_χ, see figure 14. Note that f the coupling between the galactic gas with the dark matter annihilation product depends on multiple less understood factors; composition of the shower, its energy spectrum and most likely on the properties of the dark matter particles itself. In figure 14, the coupling factor is set to $f = 0.5$, which seems to be a good average approximation over different channels by [37]. It is clear that finding these constraints for different values of f should not be a problem, and is therefore less relevant.
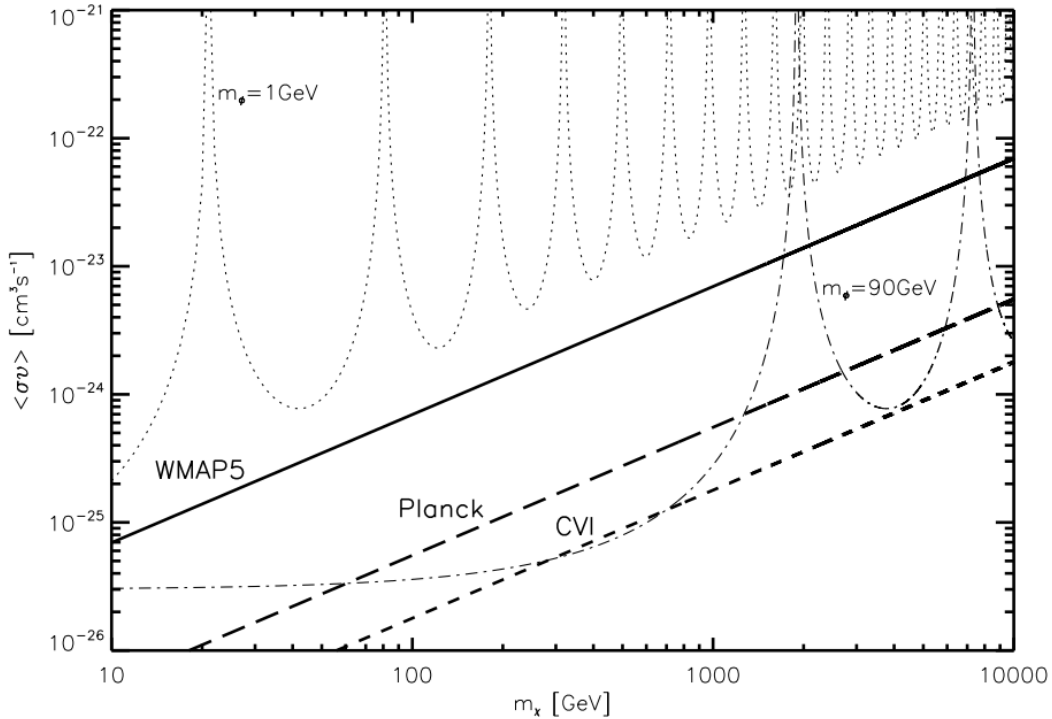
Figure 14: Figure from [37]. Velocity averaged annihilation cross-section $< \sigma v >_r$ at recombination as a function of dark matter mass m_χ, with the coupling parameter $f = 0.5$. Where the thin dashed lines are constraints from Sommerfeld enhanced cross-sections (for two different boson masses $m_\phi = 1$ GeV and $m_\phi = 90$ GeV) and the thick lines are constrains from WMAP and predicted Planck data and its Cosmic Variance Limited case.

The thin dashed lines correspond to the constrains by the Sommerfeld enhancement (SE), which enhances the self-annihilating dark matter cross-section to explain the positron excess mentioned before (see chapter 3.3). This has been plotted for two different force carrier boson masses ($m_\phi = 1 GeV$ and $m_\phi = 90 GeV$). The resonating form of the constraints is due to the Sommerfeld enhancement solution being saturated at low velocity ($\beta \sim m_\phi / m_\chi$), see formula 16.

$$SE(\beta) = \frac{\alpha \pi}{\beta} \left(1 - e^{-\alpha \pi / \beta} \right) \qquad (16)$$

The thick line describes the constrains found from the WMAP5 data (2009) [58] and their maximum likelihood fits of the parameters found in 15. It also excludes most of the Sommerfeld enhancements

in the boson mass range of a few GeV. We can summarize the WMAP5 constraints by the following upper limit cross-section:

$$\sigma v_{z_r}^{max} = 71.2 \cdot 10^{-26} \Big(\frac{p_{ann}^{max}}{2.0 \cdot 10^{-6} m^3 s^{-1} kg^{-1}} \Big) \Big(\frac{m_\chi}{100 GeV} \Big) \Big(\frac{0.5}{f} \Big) \tag{17}$$

Where $\sigma v_{z_r}^{max}$ is the upper limit on the velocity averaged self-annihilation cross-section in terms of p_{ann} equation 14, m_χ the dark matter WIMP mass and f the coupling factor.

A prediction of the probe qualities of Planck (2015) is plotted as the thick long dashed line. Planck data is discussed more in-depth below. The Cosmic Variance Limited (CVL) case with comparable angular resolution as Planck, is also plotted and denoted as the thick short dashed line. In the CVL case, the Gaussian like fluctuations of the cosmic microwave background are ignored, which almost differ a order of magnitude with the real constraints. Figure 14 also shows that for increasing dark matter mass m_χ, the cross-section also goes up as you would expect from equation 17. In the previous method of detecting dark matter (see chapter 2) we saw that probing higher masses is difficult due to a low gamma-ray flux.

3.5.1   WMAP

The Wilkinson Microwave Anisotropy Probe (WMAP) launched on a spacecraft in 2001 by NASA into a lunar assisted trajectory (see Appendix 4.1) and was the successor of COBE. It was planned to observe the CMB fluctuations for 24 months, which was subsequently extended to almost 10 years. The passively cooled microwave radiometers measure the temperature difference of the CMB between two different point in the sky and compares them directly. This method is more accurate than measuring absolute values and allows WMAP to probe up to $0.0002K$ differences over a frequency range of $23 - 94GHz$ (see NASA website [59]). Its 5 year run data (WMAP5) provides stringent constraints on the parameters of the minimal ΛCDM model [58], which are shown in figure 15. The uncertainties on these parameters are partly due to instrumental effects but largely due gravitational lensing by imhomogeneous mass distributions in or along the line of sight.

SUMMARY OF THE COSMOLOGICAL PARAMETERS OF ΛCDM MODEL AND THE CORRESPONDING 68% INTERVALS

Class	Parameter	WMAP 5-year ML[a]	WMAP+BAO+SN ML	WMAP 5-year Mean[b]	WMAP+BAO+SN Mean
Primary	$100\Omega_b h^2$	2.268	2.262	2.273 ± 0.062	$2.267^{+0.058}_{-0.059}$
	$\Omega_c h^2$	0.1081	0.1138	0.1099 ± 0.0062	0.1131 ± 0.0034
	Ω_Λ	0.751	0.723	0.742 ± 0.030	0.726 ± 0.015
	n_s	0.961	0.962	$0.963^{+0.014}_{-0.015}$	0.960 ± 0.013
	τ	0.089	0.088	0.087 ± 0.017	0.084 ± 0.016
	$\Delta_\mathcal{R}^2 (k_0{}^e)$	2.41×10^{-9}	2.46×10^{-9}	$(2.41 \pm 0.11) \times 10^{-9}$	$(2.445 \pm 0.096) \times 10^{-9}$
Derived	σ_8	0.787	0.817	0.796 ± 0.036	0.812 ± 0.026
	H_0	72.4 km/s/Mpc	70.2 km/s/Mpc	$71.9^{+2.6}_{-2.7}$ km/s/Mpc	70.5 ± 1.3 km/s/Mpc
	Ω_b	0.0432	0.0459	0.0441 ± 0.0030	0.0456 ± 0.0015
	Ω_c	0.206	0.231	0.214 ± 0.027	0.228 ± 0.013
	$\Omega_m h^2$	0.1308	0.1364	0.1326 ± 0.0063	$0.1358^{+0.0037}_{-0.0036}$
	$z_{\text{reion}}{}^f$	11.2	11.3	11.0 ± 1.4	10.9 ± 1.4
	$t_0{}^g$	13.69 Gyr	13.72 Gyr	13.69 ± 0.13 Gyr	13.72 ± 0.12 Gyr

[a]Dunkley et al. (2008). "ML" refers to the Maximum Likelihood parameters
[b]Dunkley et al. (2008). "Mean" refers to the mean of the posterior distribution of each parameter
[c]Dunkley et al. (2008). "ML" refers to the Maximum Likelihood parameters
[d]Dunkley et al. (2008). "Mean" refers to the mean of the posterior distribution of each parameter
[e]$k_0 = 0.002$ Mpc^{-1}. $\Delta_\mathcal{R}^2 (k) = k^3 P_\mathcal{R}(k)/(2\pi^2)$ (Eq. [15])
[f]"Redshift of reionization," if the universe was reionized instantaneously from the neutral state to the fully ionized state at z_{reion}
[g]The present-day age of the universe

Figure 15: Table from [58]. Maximum likelihood parameters of ΛCDM model by WMAP5, BAO and SN data set.

Some of the parameters mentioned in 15 can be directly found in figure 15; Hubble constant H_0 and h, baryonic matter density Ω_b, dark matter density Ω_c, scalar spectral index n_s and the z value of reinozation z_{reion}. Also found in [58] is the amplitude of the primordial power spectrum $A_{ps} = 0.0011 \pm 0.001 \mu K^2 sr$, they leave the parameters $< \sigma v >_r$ and m_{DM} to others.

3.5.2 Planck

The successor of WMAP is named after the German Nobel prize winner; Max Planck. It is also the first probe send by the European Space Agency (ESA) which focuses on studying the CMB. Planck launched in 2009 and orbits the second liberation point (L2) just like WMAP did, see Appendix 4.1. Furthermore, Planck observers in a frequency range of $30 - 857 GHz$ in nine frequency ranges instead of five for WMAP, which improve the astrophysical foreground models. Understanding the imhomogeneous mass distributions in and along the line of sight is quite important, since the measurement will be limited by how well the foreground can be subtracted. After a three year run, to following constraints on the ΛCDM model parameters were found [41]:

Parameter	PlanckTT+lowP 68% limits	PlanckTT, TE, EE+lowP 68% limits
$\Omega_b h^2$	0.02222 ± 0.00023	0.02225 ± 0.00016
$\Omega_c h^2$	0.1197 ± 0.0022	0.1198 ± 0.0015
$100\theta_{MC}$	1.04085 ± 0.00047	1.04077 ± 0.00032
τ	0.078 ± 0.019	0.079 ± 0.017
$\ln(10^{10}A_s)$	3.089 ± 0.036	3.094 ± 0.034
n_s	0.9655 ± 0.0062	0.9645 ± 0.0049
H_0	67.31 ± 0.96	67.27 ± 0.66
Ω_Λ	0.685 ± 0.013	0.6844 ± 0.0091
Ω_m	0.315 ± 0.013	0.3156 ± 0.0091

Figure 16: Table from [41]. Constraints on the cosmological ΛCDM model by Planck.

The results of WMAP and Planck agree with each other, but more impressive are the two to three order of magnitude improvements on the uncertainties of the parameters. Table 17 shows consistent output parameters under different maximal likelihood methods. These results also show a remarkable agreement considering different foreground approximations have been used [41].

Parameter	Plik	CamSpec	Hillipop	Mspec	Xfaster (SMICA)
$\Omega_b h^2$	0.02221 ± 0.00023	0.02224 ± 0.00023	0.02218 ± 0.00023	0.02218 ± 0.00024	0.02184 ± 0.00024
$\Omega_c h^2$	0.1203 ± 0.0023	0.1201 ± 0.0023	0.1201 ± 0.0022	0.1204 ± 0.0024	0.1202 ± 0.0023
$100\theta_{MC}$	1.0406 ± 0.00047	1.0407 ± 0.00048	1.0407 ± 0.00046	1.0409 ± 0.00050	1.041 ± 0.0005
τ	0.085 ± 0.018	0.087 ± 0.018	0.075 ± 0.019	0.075 ± 0.018	0.069 ± 0.019
$10^9 A_s e^{-2\tau}$	1.888 ± 0.014	1.877 ± 0.014	1.870 ± 0.011	1.878 ± 0.012	1.866 ± 0.015
n_s	0.962 ± 0.0063	0.965 ± 0.0066	0.961 ± 0.0072	0.959 ± 0.0072	0.960 ± 0.0071
Ω_m	0.3190 ± 0.014	0.3178 ± 0.014	0.3164 ± 0.014	0.3174 ± 0.015	0.3206 ± 0.015
H_0	67.0 ± 1.0	67.1 ± 1.0	67.1 ± 1.0	67.1 ± 1.1	66.8 ± 1.0

Notes. Each column gives the results for various high-ℓ TT likelihoods at $\ell > 50$ when combined with a prior of $\tau = 0.07 \pm 0.02$. The SMICA parameters were obtained for $\ell_{max} = 2000$.

Figure 17: Table from [41]. Constraints on the cosmological ΛCDM model with Planck data, analyzed by different maximal likelihood methods.
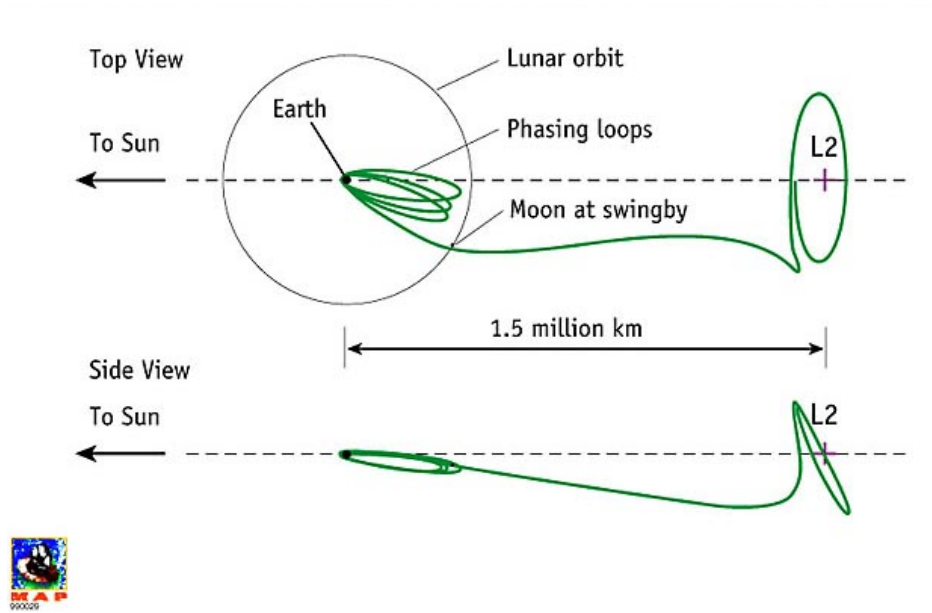
4 Appendix

4.1 Appendix A

Figure 18: Figure from NASA website. WMAP lunar assisted trajectory to the Sun-Earth L2 libration point.

References

[1] T. M. Nieuwenhuizen. Subjecting dark matter candidates to the cluster test. *ArXiv e-prints*, October 2017.

[2] A. Bottino, V. de Alfaro, N. Fornengo, G. Mignola, and S. Scopel. On the neutralino as dark matter candidate. II. Direct detection. *Astroparticle Physics*, 2:77–90, February 1994.

[3] Jennifer M. Gaskins. A review of indirect searches for particle dark matter. *Contemporary Physics*, 57(4):496–525, 2016.

[4] Marco Cirelli, Gennaro Corcella, Andi Hektor, Gert Hütsi, Mario Kadastik, Paolo Panci, Martti Raidal, Filippo Sala, and Alessandro Strumia. Pppc 4 dm id: a poor particle physicist cookbook for dark matter indirect detection. *Journal of Cosmology and Astroparticle Physics*, 2011(03):051, 2011.

[5] A. Abramowski, F. Aharonian, F. Ait Benkhali, A. G. Akhperjanian, E. Angüner, M. Backes, S. Balenderan, A. Balzer, A. Barnacka, Y. Becherini, and et al. Search for dark matter annihilation signatures in H.E.S.S. observations of dwarf spheroidal galaxies. , 90(11):112012, December 2014.

[6] Fabio Iocco, Miguel Pato, Gianfranco Bertone, and Philippe Jetzer. Dark matter distribution in the milky way: microlensing and dynamical constraints. *Journal of Cosmology and Astroparticle Physics*, 2011(11):029, 2011.

[7] Frank C. van den Bosch and Rob A. Swaters. Dwarf galaxy rotation curves and the core problem of dark matter haloes. *Monthly Notices of the Royal Astronomical Society*, 325(3):1017–1038, 2001.

[8] J. Diemand, M. Kuhlen, P. Madau, M. Zemp, B. Moore, D. Potter, and J. Stadel. Clumps and streams in the local dark matter distribution. , 454:735–738, August 2008.

[9] Mattia Fornasa and Anne M Green. Self-consistent phase-space distribution function for the anisotropic dark matter halo of the milky way. *Physical Review D*, 89(6):063531, 2014.

[10] Paolo Gondolo and Joseph Silk. Dark matter annihilation at the galactic center. *Physical Review Letters*, 83(9):1719, 1999.

[11] Oleg Y Gnedin, Andrey V Kravtsov, Anatoly A Klypin, and Daisuke Nagai. Response of dark matter halos to condensation of baryons: cosmological simulations and improved adiabatic contraction model. *The Astrophysical Journal*, 616(1):16, 2004.

[12] Oleg Y Gnedin, Daniel Ceverino, Nickolay Y Gnedin, Anatoly A Klypin, Andrey V Kravtsov, Robyn Levine, Daisuke Nagai, and Gustavo Yepes. Halo contraction effect in hydrodynamic simulations of galaxy formation. *arXiv preprint arXiv:1108.5736*, 2011.

[13] B. Moore, T. Quinn, F. Governato, J. Stadel, and G. Lake. Cold collapse and the core catastrophe. , 310:1147–1152, December 1999.

[14] J. J. Adams, J. D. Simon, M. H. Fabricius, R. C. E. van den Bosch, J. C. Barentine, R. Bender, K. Gebhardt, G. J. Hill, J. D. Murphy, R. A. Swaters, J. Thomas, and G. van de Ven. Dwarf Galaxy Dark Matter Density Profiles Inferred from Stellar and Gas Kinematics. , 789:63, July 2014.

[15] J. F. Navarro, E. Hayashi, C. Power, A. R. Jenkins, C. S. Frenk, S. D. M. White, V. Springel, J. Stadel, and T. R. Quinn. The inner structure of ΛCDM haloes - III. Universality and asymptotic slopes. , 349:1039–1051, April 2004.

[16] Liang Gao, Julio F Navarro, Shaun Cole, Carlos S Frenk, Simon DM White, Volker Springel, Adrian Jenkins, and Angelo F Neto. The redshift dependence of the structure of massive λ cold dark matter haloes. *Monthly Notices of the Royal Astronomical Society*, 387(2):536–544, 2008.

[17] J. F. Navarro, A. Ludlow, V. Springel, J. Wang, M. Vogelsberger, S. D. M. White, A. Jenkins, C. S. Frenk, and A. Helmi. The diversity and similarity of simulated cold dark matter haloes. , 402:21–34, February 2010.

[18] J. Einasto. On the Construction of a Composite Model for the Galaxy and on the Determination of the System of Galactic Parameters. *Trudy Astrofizicheskogo Instituta Alma-Ata*, 5:87–100, 1965.

[19] Gianfranco Bertone, Andrew R Zentner, and Joseph Silk. New signature of dark matter annihilations: Gamma rays from intermediate-mass black holes. *Physical Review D*, 72(10):103517, 2005.

[20] WB Atwood, Aous A Abdo, Markus Ackermann, W Althouse, B Anderson, M Axelsson, L Baldini, J Ballet, DL Band, Guido Barbiellini, et al. The large area telescope on the fermi gamma-ray space telescope mission. *The Astrophysical Journal*, 697(2):1071, 2009.

[21] Markus Ackermann, Marco Ajello, WB Atwood, Luca Baldini, Guido Barbiellini, D Bastieri, K Bechtol, R Bellazzini, RD Blandford, ED Bloom, et al. Constraints on the galactic halo dark matter from fermi-lat diffuse measurements. *The Astrophysical Journal*, 761(2):91, 2012.

[22] Andrea Albert, Brandon Anderson, Keith Bechtol, Alex Drlica-Wagner, Manuel Meyer, Miguel Sánchez-Conde, L Strigari, M Wood, TMC Abbott, Filipe B Abdalla, et al. Searching for dark matter annihilation in recently discovered milky way satellites with fermi-lat. *The Astrophysical Journal*, 834(2):110, 2017.

[23] M Ackermann, A Albert, Brandon Anderson, WB Atwood, L Baldini, G Barbiellini, D Bastieri, K Bechtol, R Bellazzini, E Bissaldi, et al. Searching for dark matter annihilation from milky way dwarf spheroidal galaxies with six years of fermi large area telescope data. *Physical Review Letters*, 115(23):231301, 2015.

[24] Gary Steigman, Basudeb Dasgupta, and John F Beacom. Precise relic wimp abundance and its impact on searches for dark matter annihilation. *Physical Review D*, 86(2):023506, 2012.

[25] Felix Aharonian, AG Akhperjanian, AR Bazer-Bachi, M Beilicke, Wystan Benbow, David Berge, K Bernlöhr, C Boisson, Oliver Bolz, V Borrel, et al. Hess observations of the galactic center region and their possible dark matter interpretation. *Physical Review Letters*, 97(22):221102, 2006.

[26] A Abramowski, Fabio Acero, F Aharonian, AG Akhperjanian, G Anton, A Barnacka, U Barres De Almeida, AR Bazer-Bachi, Yvonne Becherini, J Becker, et al. Search for a dark matter annihilation signal from the galactic center halo with hess. *Physical Review Letters*, 106(16):161301, 2011.

[27] H. Abdallah et al. Search for γ-Ray Line Signals from Dark Matter Annihilations in the Inner Galactic Halo from 10 Years of Observations with H.E.S.S. *Phys. Rev. Lett.*, 120(20):201101, 2018.

[28] S Archambault, A Archer, W Benbow, R Bird, E Bourbeau, T Brantseg, M Buchovecky, JH Buckley, V Bugaev, K Byrum, et al. Dark matter constraints from a joint analysis of dwarf spheroidal galaxy observations with veritas. *Physical Review D*, 95(8):082001, 2017.

[29] Max L Ahnen, S Ansoldi, LA Antonelli, C Arcaro, D Baack, A Babić, B Banerjee, P Bangale, U Barres de Almeida, JA Barrio, et al. Indirect dark matter searches in the dwarf satellite galaxy ursa major ii with the magic telescopes. *Journal of Cosmology and Astroparticle Physics*, 2018(03):009, 2018.

[30] AU Abeysekara, A Albert, R Alfaro, C Alvarez, R Arceo, JC Arteaga-Velázquez, D Avila Rojas, HA Ayala Solares, A Becerril, E Belmont-Moreno, et al. A search for dark matter in the galactic halo with hawc. *Journal of Cosmology and Astroparticle Physics*, 2018(02):049, 2018.

[31] The Cherenkov Telescope Array Consortium, BS Acharya, I Agudo, I Al Samarai, R Alfaro, J Alfaro, C Alispach, R Alves Batista, J-P Amans, E Amato, et al. Science with the cherenkov telescope array. *arXiv preprint arXiv:1709.07997*, 2017.

[32] The CTA Consortium. Design concepts for the cherenkov telescope array. *arXiv preprint arXiv:1008.3703*, 2010.

[33] Hamish Silverwood, Christoph Weniger, Pat Scott, and Gianfranco Bertone. A realistic assessment of the cta sensitivity to dark matter annihilation. *Journal of Cosmology and Astroparticle Physics*, 2015(03):055, 2015.

[34] O Adriani, Y Akaike, K Asano, Y Asaoka, MG Bagliesi, G Bigongiari, WR Binns, S Bonechi, M Bongi, JH Buckley, et al. The calorimetric electron telescope (calet) for high-energy astroparticle physics on the international space station. In *Journal of Physics: Conference Series*, volume 632, page 012023. IOP Publishing, 2015.

[35] NP Topchiev, AM Galper, V Bonvicini, O Adriani, RL Aptekar, IV Arkhangelskaja, AI Arkhangelskiy, AV Bakaldin, L Bergstrom, E Berti, et al. Gamma-400 gamma-ray observatory. *arXiv preprint arXiv:1507.06246*, 2015.

[36] Xiaoyuan Huang, Anna S Lamperstorfer, Yue-Lin Sming Tsai, Ming Xu, Qiang Yuan, Jin Chang, Yong-Wei Dong, Bing-Liang Hu, Jun-Guang Lü, Le Wang, et al. Perspective of monochromatic gamma-ray line detection with the high energy cosmic-radiation detection (herd) facility onboard china's space station. *Astroparticle Physics*, 78:35–42, 2016.

[37] Silvia Galli, Fabio Iocco, Gianfranco Bertone, and Alessandro Melchiorri. Cmb constraints on dark matter models with large annihilation cross section. *Physical Review D*, 80(2):023505, 2009.

[38] Antony Lewis, Jochen Weller, and Richard Battye. The cosmic microwave background and the ionization history of the universe. *Monthly Notices of the Royal Astronomical Society*, 373(2):561–570, 2006.

[39] Silvia Galli, Rachel Bean, Alessandro Melchiorri, and Joseph Silk. Delayed recombination and cosmic parameters. *Phys. Rev. D*, 78:063532, Sep 2008.

[40] Jaiseung Kim and Pavel Naselsky. Accelerated recombination, and the acbar and wmap data. *The Astrophysical Journal Letters*, 678(1):L1, 2008.

[41] N Aghanim, M Arnaud, M Ashdown, J Aumont, C Baccigalupi, AJ Banday, RB Barreiro, JG Bartlett, N Bartolo, E Battaner, et al. Planck 2015 results-xi. cmb power spectra, likelihoods, and robustness of parameters. *Astronomy & Astrophysics*, 594:A11, 2016.

[42] Le Zhang, Xuelei Chen, Yi-An Lei, and Zong-guo Si. Impacts of dark matter particle annihilation on recombination and the anisotropies of the cosmic microwave background. *Physical Review D*, 74(10):103519, 2006.

[43] A Lewis, A Challinor, and A Lasenby. Efficient computation of cmb anisotropies in closed frw models. *Astrophys. J*, 538:473, 2000.

[44] Sara Seager, Dimitar D Sasselov, and Douglas Scott. How exactly did the universe become neutral? *The Astrophysical Journal Supplement Series*, 128(2):407, 2000.

[45] PJE Peebles. Recombination of the primeval plasma. *The Astrophysical Journal*, 153:1, 1968.

[46] Nikhil Padmanabhan and Douglas P Finkbeiner. Detecting dark matter annihilation with cmb polarization: Signatures and experimental prospects. *Physical Review D*, 72(2):023508, 2005.

[47] O Adriani, GC Barbarino, GA Bazilevskaya, R Bellotti, M Boezio, EA Bogomolov, L Bonechi, M Bongi, V Bonvicini, S Bottai, et al. Observation of an anomalous positron abundance in the cosmic radiation. *arXiv preprint arXiv:0810.4995*, 2008.

[48] Ilias Cholis, Douglas P Finkbeiner, Lisa Goodenough, and Neal Weiner. The pamela positron excess from annihilations into a light boson. *Journal of Cosmology and Astroparticle Physics*, 2009(12):007, 2009.

[49] Massimiliano Lattanzi and Joseph Silk. Can the wimp annihilation boost factor be boosted by the sommerfeld enhancement? *Physical Review D*, 79(8):083523, 2009.

[50] Jesus Zavala, Mark Vogelsberger, and Simon DM White. Relic density and cmb constraints on dark matter annihilation with sommerfeld enhancement. *Physical Review D*, 81(8):083502, 2010.

[51] Tracy R. Slatyer. Indirect dark matter signatures in the cosmic dark ages. I. Generalizing the bound on s -wave dark matter annihilation from Planck results. *Physical Review D*, 93(2):023527, jan 2016.

[52] Mathew S. Madhavacheril, Neelima Sehgal, and Tracy R. Slatyer. Current dark matter annihilation constraints from CMB and low-redshift data. *Physical Review D*, 89(10):103508, may 2014.

[53] Sara Seager, Dimitar D. Sasselov, and Douglas Scott. RECFAST: Calculate the Recombination History of the Universe. *Astrophysics Source Code Library, record ascl:1106.026*, 2011.

[54] G. Hütsi, J. Chluba, A. Hektor, and M. Raidal. WMAP7 and future CMB constraints on annihilating dark matter: implications for GeV-scale WIMPs. *Astronomy & Astrophysics*, 535:A26, nov 2011.

[55] D Larson, J Dunkley, G Hinshaw, Eiichiro Komatsu, MR Nolta, CL Bennett, B Gold, M Halpern, RS Hill, N Jarosik, et al. Seven-year wilkinson microwave anisotropy probe (wmap*) observations: power spectra and wmap-derived parameters. *The Astrophysical Journal Supplement Series*, 192(2):16, 2011.

[56] D. J. Eisenstein, I. Zehavi, D. W. Hogg, R. Scoccimarro, M. R. Blanton, R. C. Nichol, R. Scranton, H. Seo, M. Tegmark, Z. Zheng, S. Anderson, J. Annis, N. Bahcall, J. Brinkmann, S. Burles, F. J. Castander, A. Connolly, I. Csabai, M. Doi, M. Fukugita, J. A. Frieman, K. Glazebrook, J. E. Gunn, J. S. Hendry, G. Hennessy, Z. Ivezic, S. Kent, G. R. Knapp, H. Lin, Y. Loh, R. H. Lupton, B. Margon, T. McKay, A. Meiksin, J. A. Munn, A. Pope, M. Richmond, D. Schlegel, D. Schneider, K. Shimasaku, C. Stoughton, M. Strauss, M. SubbaRao, A. S. Szalay, I. Szapudi, D. Tucker, B. Yanny, and D. York. Detection of the Baryon Acoustic Peak in the Large-Scale Correlation Function of SDSS Luminous Red Galaxies. jan 2005.

[57] Laura Lopez-Honorez, Olga Mena, Sergio Palomares-Ruiz, and Aaron C Vincent. Constraints on dark matter annihilation from CMB observations before Planck. *Journal of Cosmology and Astroparticle Physics*, 2013(07):046–046, jul 2013.

[58] E. Komatsu, J. Dunkley, M. R. Nolta, C. L. Bennett, B. Gold, G. Hinshaw, N. Jarosik, D. Larson, M. Limon, L. Page, D. N. Spergel, M. Halpern, R. S. Hill, A. Kogut, S. S. Meyer, G. S. Tucker, J. L. Weiland, E. Wollack, and E. L. Wright. Five-Year Wilkinson Microwave Anisotropy Probe Observations: Cosmological Interpretation. , 180:330–376, February 2009.

[59] NASA. https://wmap.gsfc.nasa.gov/. 2001.

4.2 Review papers

https://arxiv.org/pdf/1707.06277.pdf WIMP dark matter candidates and searches – current status and future prospects

Indirect detection of dark matter - Lars Bergstrom (2007)

J. M. Gaskins, A review of indirect searches for particle dark matter, Contemp. Phys. (2016) https://arxiv.org/pdf/1604.00014.pdf

Indirect detection of dark matter - J. Carr et al. (2006)

Ackerman et al. (2015) ; *"Searching for Dark Matter Annihilation from Milky Way Dwarf Spheroidal Galaxies with Six Years of Fermi Large Area Telescope Data"*

4.3 Scale Radii

M. A. Breddels and A. Helmi, "Model comparison of the dark matter profiles of Fornax, Sculptor, Carina and Sextans", A&A 559, 10 p., (2013) https://arxiv.org/pdf/1304.2976.pdf

4.4 ID DM signal radiative transfer

Profumo, S. and Jeltema, E.T. (2011) ; *"Extragalactic Inverse Compton Light from Dark Matter annihilation and the Pamela positron excess"* http://iopscience.iop.org/article/10.1088/1475-7516/2009/07/020/meta